Chinese Chemical Letters 34 (2023) 107119

Contents lists available at ScienceDirect

Chinese Chemical Letters

journal homepage: www.elsevier.com/locate/cclet

Phase engineering two-dimensional nanostructures for electrocatalytic hydrogen evolution reaction

Zhongshui Li[a], Yang Yue[a], Junchen Peng[a], Zhimin Luo[b,*]

[a] College of Chemistry & Materials Science, Fujian Normal University, Fuzhou 350007, China
[b] Key Laboratory for Organic Electronics and Information Displays & Jiangsu Key Laboratory for Biosensors, Institute of Advanced Materials (IAM), Jiangsu National Synergetic Innovation Center for Advanced Materials (SICAM), Nanjing University of Posts and Telecommunications, Nanjing 210023, China

ARTICLE INFO

Article history:
Received 15 November 2021
Revised 19 December 2021
Accepted 7 January 2022
Available online 13 January 2022

Keywords:
Two-dimensional nanomaterials
Phase engineering
Hydrogen evolution reaction
Electrocatalysis
Transition metal dichalcogenides
Metal thiophosphates
2D noble metal nanomaterials

ABSTRACT

Hydrogen (H_2) is considered to be a promising substitute for fossil fuels. Two-dimensional (2D) nanomaterials have exhibited an efficient electrocatalytic capacity to catalyze hydrogen evolution reaction (HER). Particularly, phase engineering of 2D nanomaterials is opening a novel research direction to endow 2D nanostructures with fascinating properties for deep applications in catalyzing HER. In this review, we briefly summarize the research progress and present the current challenges on phase engineering of 2D nanomaterials for their applications in electrocatalytic HER. Our summary will be of significance to provide fundamental understanding for designing novel 2D nanomaterials with unconventional phases to electrochemically catalyze HER.

1. Introduction

The continuous consumption of fossil fuels has given rise to the serious energy and environmental crises, which severely hindered the sustainable development of mankind [1–3]. In the past few decades, great progress has been made in sustainable and clean energy, such as hydrogen, solar and biomass energy [4–7]. Hydrogen (H_2), as a clean, economical and renewable energy source, has a highest energy density (142 MJ/kg) among all chemical fuels and is considered a promising substitute for fossil fuels [8–13]. In industry, H_2 is mainly produced through the steam-reforming reaction under harsh conditions, resulting in the emission of greenhouse gasses and pollutants [8,14-17]. Electrochemical hydrogen evolution reaction (HER) is one of sustainable and promising ways to produce hydrogen on a large scale, in which electrocatalysts are the key factor to reduce electrochemical reaction activation energy for HER [4,18-23].

The electrocatalytic HER process on the surface of electrodes includes three separate steps: the adsorption of hydrogen ions (the Volmer step), the formation of hydrogen molecules (the Heyrovsky or the Tafel step), and the desorption of the generated H_2 [14,24]. Depending on the protons deriving from the different medium, the two-electron transfer reaction of HER follows the different pathways. In acidic medium, an adsorbed hydrogen atom (H^*) is formed in the Volmer step, when a proton (H^+) adsorbed on an electrocatalytic active site (*) is coupled with an electron (e^-), and the process is assigned as $H^+\ (aq) + {}^* + e^- \rightarrow H^*\ (ads)$ [24,25]. The subsequent production of H_2 takes place *via* either the chemical combination of two surface adsorbed hydrogen atoms or the direct bonding of a hydrated proton, a transferred electron and an adsorbed hydrogen atom [24,26]. The former one is known as the Tafel reaction step [$H^*\ (ads) + H^*\ (ads) \rightarrow H_2\ (gas)$], and the latter one is called the Heyrovsky reaction step [$H^+\ (aq) + e^- + H^*\ (ads) \rightarrow H_2\ (gas)$] [24,27]. As for an alkaline medium, the Volmer and the Heyrovsky reactions are presented as $H_2O + * + e^- \rightarrow H^*\ (ads) + OH^-$ and $H_2O + e^- + H^*\ (ads) \rightarrow H_2\ (gas) + OH^-$, respectively [14,24]. The third step is the desorption of the generated H_2 (gas) molecules from the surface of electrocatalysts. It should be noted that the adoption of electrocatalysts for HER is in favor of improving the energy-conversion efficiency, particularly harvesting a higher current density at a lower overpotential.

Two-dimensional (2D) nanomaterials, such as transition metal dichalcogenides (TMDs), metal thiophosphates (MTPs), and 2D noble metal nanomaterials, generally possess a sheet-like structure with a thickness of a single or few atomic layers [25,28-36]. Due to their atomic thickness, high anisotropy and electron confinement in two dimensions, 2D nanomaterials possess strikingly fascinating physicochemical properties and attract tremendous research inter-

---

* Corresponding author.
E-mail address: iamzmluo@njupt.edu.cn (Z. Luo).

https://doi.org/10.1016/j.cclet.2022.01.012

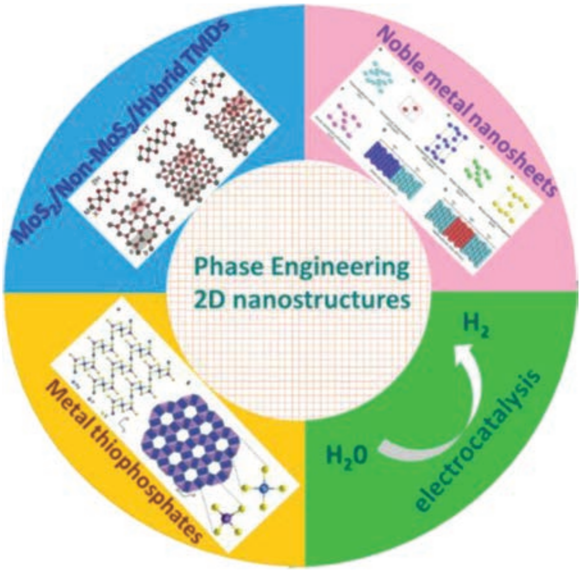

Fig. 1. Overview of this review.

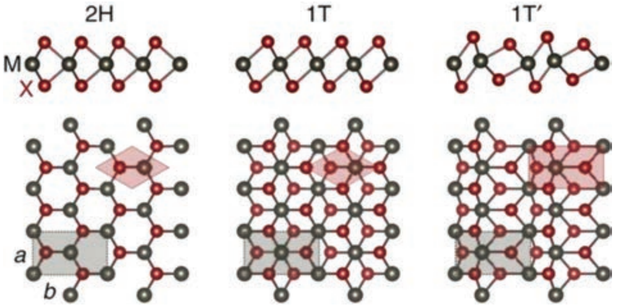

Fig. 2. Three crystal structures of monolayer TMDs. The top and bottom schematics show cross-sectional views and basal plane views, respectively. In all three phases, a layer of transition metal atoms (M, gray atoms) is sandwiched between two chalcogenide layers (X, red atoms). Reproduced with permission [73]. Copyright 2016, Springer Nature.

ests especially for electrochemical HER [35,37-44]. Currently, more and more novel graphene-analogous 2D materials have been explored as efficient electrocatalysts for HER, because they can provide moderate binding between the active sites (*) and adsorbed H atoms in the intermediate H* (ads), to facilitate the HER process. Although some exciting achievements in electrochemical HER of 2D nanomaterials have been obtained, challenges on designing and synthesizing highly efficient electrocatalysts for HER still exist [36,37,45-48]. Precisely controlling the compositions, thicknesses, crystal phases, vacancies and surface properties of 2D nanomaterials is important to unveil the correlations between their structural features and catalytic properties [34,49-52]. Fortunately, phase engineering has been considered as a fantastic and effective strategy to adjust the intrinsic physicochemical properties of 2D nanomaterials and realize the precise preparation of highly efficient electrocatalysts [24,26,53-55]. The intriguing structures and properties of 2D nanomaterials deriving from phase engineering of 2D nanomaterials open new places in the applications of electrochemical HER [14,26,27,56-58]. Therefore, it is necessary to summarize recent advances on the phase engineering of 2D nanomaterials-based catalysts and their applications in electrocatalytic hydrogen evolution.

Herein, this mini review is focused on the phase engineering control on TMDs (MoS_2, non-MoS_2 TMDs, and TMDs hybrids), MTPs and 2D noble metal nanostructures (Au-based and non-Au based) for electrocatalytic HER (Fig. 1). The challenges and perspectives on the application of phase engineering 2D nanomaterials in electrocatalytic HER are also presented.

2. TMDs

2.1. MoS_2

TMDs, one of the typical graphene-analogous 2D materials, have attracted considerable attention in recent years because of their unique properties and promising applications in electrochemical energy storage and conversion [13,15,59-62]. However, the limited number of active sites as well as blocked ion and mass transport severely impair their electrochemical performance. A common feature of these materials lies in their tunable functional properties that closely correlate to their shape and composition, especially to their crystal phases [20,63-65]. Therefore, phase engineering of nanomaterials can be an effective strategy to tune the promising properties of TMDs for electrocatalyzing HER [26,53,66-68]. Molybdenum (Mo)-based compounds generally exhibit superior electrocatalysis towards HER [69–72], especially, MoS_2 is the typical representative of this family [12,73-80]. Fig. 2 illustrates the most well-known three crystal phases of MoS_2, including 2H, 1T and 1T′ phase [15,24,63,73,81]. These three crystal phases present a lamellar structure with one layer of Mo sandwiched between two layers of S. Hexagonal 2H phase with S atom in trigonal prismatic coordination (D_{3h}) around Mo atom exhibits a good stability. Metallic 1T phase is a one-layer stack in the tetragonal symmetry with octahedral coordination (D_{3d}) [82]. Distorted 1T phase with Mo atoms bonded in the form of zigzag chains is called 1T′ phase [24,73]. Conversion among three phases could take place with geometric rotations [24,55]. The HER active sites of 2H-MoS_2 locate at sulfur edges with the zigzag or armchair distribution, however, the inert basal plane and the semiconducting feature of 2H MoS_2 limit their HER performance. By contrast, as for 1T/1T′-MoS_2, both their edges and basal planes are electrocatalytically active. Particularly, the metallic characteristic and larger surface area of 2D 1T/1T′-MoS_2 ensure the fast transfer of electrons and the large abundance of active sites, respectively. Thereby, 1T/1T′ TMDs have been regarded as promising alternatives to Pt for industry-level HER [24,26,53,83].

Currently, a straightforward way to improve the catalytic properties is to transform 2H phase TMDs into metallic 1T or 1T′ phase TMDs *via* phase engineering of nanomaterials [59,84]. For example, Lukowski *et al.* reported that metallic 1T-MoS_2 could greatly improve the HER catalytic performance. They firstly synthesized 2H phase flower-like MoS_2 nanostructures with a high density of exposed edges directly on graphite substrates *via* a simple chemical vapor deposition (CVD) method with molybdenum (V) chloride and sulfur powder as precursors. After that, they converted the multilayered semiconductive 2H-MoS_2 nanostructures into metallic 1T-MoS_2 by simply soaking them in *n*–butyl lithium solution. It is found that 1T-MoS_2 exhibited facile electrode kinetics and low-loss electrical transport with a Tafel slope of 43 mV/dec. Importantly, the catalytic performance of 1T-MoS_2 nanosheets was stable and there was a less than 15% decay of electrocatalytic current density after 1000 cycles [85]. Park *et al.* adopted a scalable method to synthesize 1T phase MoS_2 *via* the molten-metal-assisted intercalation (MMI) approach, in which highly reactive molten potassium metal can intercalate into the MoS_2 interlayers to induce an efficient phase transition from the 2H to 1T crystal phase. Due to the high purity and stability of 1T phase, 1T-MoS_2 (MMI) gave a higher electrocatalytic performance for HER than 2H-MoS_2 [20]. 1T′ phase which is different from the 2H and 1T structures presents different types of chalcogen atoms in the crystal space in terms of the positions, so the highly asymmetric 1T′ phase TMDs may re-

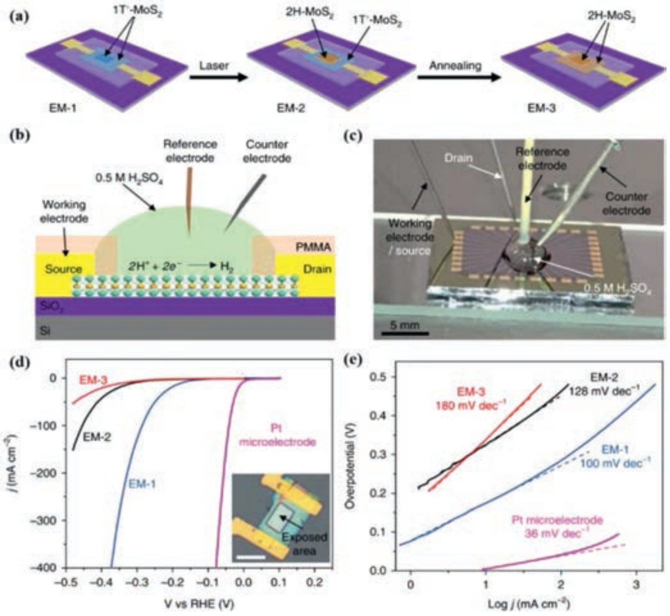

Fig. 3. Phase-dependent HER measurements in electrochemical microcells. (a) Schematic of fabricating three types of electrochemical microcell (EM-1, EM-2 and EM-3). (b) Electrochemical set-up for electrocatalytic HER measurements on electrochemical microcells. (c) Photograph of electrochemical set-up for electrocatalytic HER measurements on electrochemical microcells. (d) Polarization curves obtained with EM-1, EM-2 and EM-3. Inset: optical microscope image of EM-1. Scale bar, 20 µm. (e) Tafel plots obtained from the polarization curves in (d). Reproduced with permission [86]. Copyright 2018, Springer Nature.

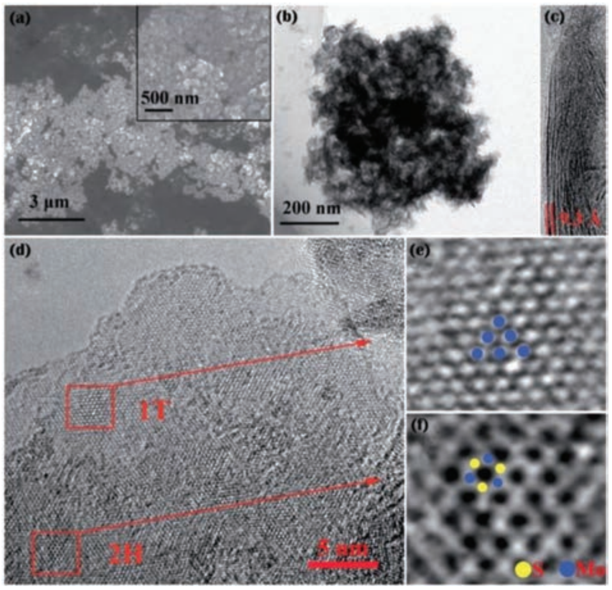

Fig. 4. (a) SEM, (b) TEM and (c, d) HRTEM images of prepared 1T/2H-MoS_2, and (e, f) HRTEM images of the region enclosed by red square of (d). Reproduced with permission [87]. Copyright 2017, Royal Society of Chemistry.

sult in different types of anionic vacancies. The vacancy can further induce the enhancement of catalytic performance and is in favor of exploiting its potential catalytic capacity. For instance, Yu *et al.* presented a facile method for crystal phase-controlled synthesis of 1T′-MoX_2 crystals with the lateral size up to hundreds of micrometers. It is revealed that 1T′-MoS_2 crystals featured a distorted octahedral coordination structure and were convertible to 2H-MoS_2 following thermal annealing or laser irradiation. Electrochemical microcells with 1T′ or 2H-MoS_2 as the working electrode were fabricated (EM-1, EM-2 and EM-3). Compared to 2H-MoS_2, 1T′-MoS_2 (EM-1) showed higher efficiency for electrochemical HER with an onset overpotential of only 65 mV and a current density of 607 mA/cm^2 at an overpotential of 400 mV (*vs.* RHE) (Fig. 3). It is found that good HER performance of 1T′-MoS_2 originated from its higher catalytic activity on the basal plane, better charge transport ability and higher anionic vacancies [86]. Since the surface energy in 1T/1T′ phase is relatively high, it is difficult to prepare MoS_2 with a pure unconventional phase. So it is necessary to tune the balance between 1T/1T′ unconventional phase and 2H pristine phase. For example, Zhang *et al.* reported an efficient hydrothermal route to prepare 1T/2H-MoS_2 catalysts using ionic liquid (*n*–butyl pyridinium bromide, [BPy]Br) as a structure-directing agent, where the large steric hindrance of [BPy]Br and mutual π stacking interaction induced phase transition of MoS_2 from 2H to 1T phase. By adding a suitable amount of [BPy]Br in the reaction system, the percentage of 1T phase in 1T/2H-MoS_2 was increased, which can expose more active sites on its basal planes/edges as well as facilitate charge transfer for HER. 1T/2H-MoS_2 with 1T percentage of 91.9% exhibited a significantly enhanced HER activity as compared to MoS_2 synthesized without the aid of [BPy]Br [67]. Wang *et al.* adopted a hydrothermal method with the addition of ammonium bicarbonate to realize the fabrication *in-situ* of the 1T phase of MoS_2, in which ammonium bicarbonate was decomposed into small molecules and ions as guests (including NH_4^+, H_2O and CO_2). These guests were inserted into the lamellar structures of MoS_2 to induce the formation of multiphasic 1T/2H-MoS_2 (Fig. 4). The existence of 1T phase provided more active sites and better conductivity for HER, resulting in a superior HER performance with a small Tafel slope of 46 mV/dec. The integration with 2H phase was beneficial for stabilization of metastable 1T phase, ensuring excellent durability of 1T/2H-MoS_2 [87]. Engineering crystal phase of MoS_2 to activate its basal planes/edges and simultaneously improve its electronic conductivity is another effective strategy for enhancing HER activity. For example, He *et al.* adopted Au-quantum-dots (QDs)-assisted vapor-phase growth to fabricate wafer-size atomically thin TMD films (MoS_2, *etc.*) with sub-10 nm grains which demonstrated an ultra-high-density grain boundaries (GBs) (up to ~1012 cm^{-2}). Experimental evidence as well as phase-field simulations indicated that the Au QDs regulated the formation of the TMD grains, resulting in enhanced electronic conductivity. This kind of MoS_2 nanograin film exhibited a superior HER performance with an onset potential of 25 mV and a Tafel slope of 54 mV/dec, indicating a good intrinsic activation of GB-rich 2D basal plane [88].

2.2. Non-MoS_2 TMDs

Besides MoS_2, other TMDs such as $MoSe_2$, MoSSe, $MoTe_2$, ReS_2, ReSSe, $ReSe_2$, SnS_2, are also widely studied [16,30,89,90]. Many non-MoS_2 TMDs also held great potentials and attracted more attention as a promising HER electrocatalyst due to their high activity and good chemical stability [91]. For example, Tan *et al.* combined the ball milling and chemical Li-intercalation to realize the large-scale production of water-dispersed and high-percentage 1T phase TMD nanodots with high-density exposed active edge sites, including WS_2, $MoSe_2$, and MoSSe, *etc.* The prepared non-MoS_2 TMD nanodots exhibited much enhanced electrochemical HER activities in acid medium as compared to their corresponding nanosheets. Due to alloying effect and Se vacancy, MoSSe nanodots exhibited better HER performance than MoS_2 nanodots, yielding a low overpotential of −140 mV at current density of 10 mA/cm^2 and a Tafel slope of 40 mV/dec [89]. By combining chemical vapor transport (CVT) and chemical Li-intercalation method, Lai *et al.* realized the large-scale production of water-dispersed and in-

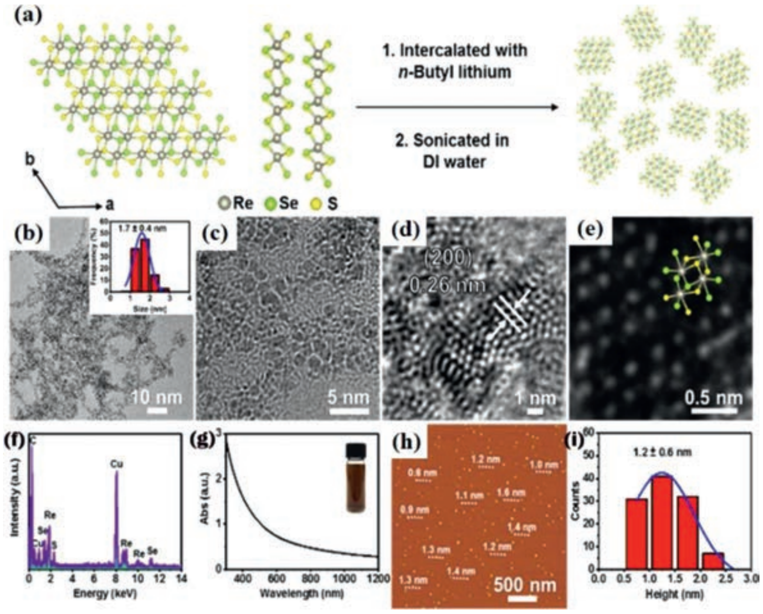

Fig. 5. Schematic diagram of the synthetic procedure and characterizations of ReSSe NDs. (a) Simulated structure of ReSSe and schematic diagram of the synthetic process of ReSSe NDs. (b) Low-magnification TEM image of the prepared ReSSe NDs. Inset: Size distribution of ReSSe NDs. (c) HRTEM image of the prepared ReSSe NDs. (d) HRTEM image of individual ReSSe NDs. (e) HAADF-STEM image of a single ReSSe nanodot showing typical 1T′ structure overlapped with the simulated structure. (f) EDS spectra of the prepared ReSSe NDs obtained under TEM mode. (g) UV−vis spectrum of the diluted solution of ReSSe NDs. Inset: Photograph of the ReSSe ND solution. (h) AFM image of the prepared ReSSe NDs. (i) Statistical analysis of the height of 110 ReSSe NDs measured from AFM images. Reproduced with permission [92]. Copyright 2018, American Chemical Society.

herent 1T′ phase $ReS_{2x}Se_{2(1-x)}$ nanodendrites (NDs) (Fig. 5). Due to their intrinsic distorted 1T′ structure, alloying effect, and unsaturated coordinated *Re* sites, the obtained ReSSe NDs exhibited superior HER performance with a low overpotential of 84 mV at a current density of 10 mA/cm^2 and a Tafel slope of 50.1 mV/dec [92]. Li *et al.* presented a facile method to synthesize high-quality WTe_2 nanoribbons crystals with 1T′ phase, in which WO_{3-x} nanoribbons was prepared through a hydrothermal method and then WO_{3-x} nanoribbons was tellurized in a CVD system. They found that highly crystallined 1T′-WTe_2 nanoribbons can be prepared on a large scale by using above two-step method and the resultant morphology of WTe_2 crystal can be tuned by regulating the first step. Electrochemical tests showed that WTe_2 nanoribbons exhibited lower overpotential and better HER performance than other tungsten-based sulfide and selenide (WS_2, WSe_2) nanoribbons. WTe_2 nanoribbons exhibited a Tafel slope of 57 mV/dec, which was about 2 and 4 times smaller than that for 2H-WS_2 nanoribbons (135 mV/dec) and 2H-WSe_2 nanoribbons (213 mV/dec), respectively. Its high HER performance was attributed to the high conductivity of semi-metallic 1T′ phase-stable WTe_2 nanoribbons, with one or two order higher charge-transfer rate than normally semiconducting 2H-stable WS_2 and WSe_2 nanoribbons [93]. Shape engineering also plays a crucial role in modulating physicochemical property of TMDs. For example, Shao *et al.* adopted a controllable growth method to synthesize the uniform monolayer 1T-SnS_2 through a CVD process on SiO_2/Si substrate. The Sn source became a key factor in controlling morphologies with different fractal dimensions. Especially, potassium halides were preferable for obtaining 1T phase SnS_2 rather than sodium halides. Density functional theory (DFT) calculations further indicated that potassium ions can effectively promote the uniform growth of 2D 1T phase SnS_2 by reducing the surface migration barrier of SnS_2 cluster and enhancing the SnS_2 adhesion force with substrate. Different morphologies of SnS_2 flakes with fractal dimensions from 1.01 to 1.81 can be precisely controlled and synthesized by adjusting reaction temperature, flow rate, and precursor stoichiometric ratio (Fig. 6). Especially, more branched SnS_2 with higher fractal dimension can provide more active sites for HER in comparison with SnS_2 of other morphologies [94].

2.3. TMDs hybrids

Multicomponent hybrid nanostructures have tunable and synergistic properties due to the electronic transfer and interaction among multiple components [61,95-99]. Design and construction of TMDs heterostructures is an effective strategy to improve their electrocatalytic properties. For instance, Rahul *et al.* fabricated the heterostructures of $MoSe_2$/WSe_2 nanosheets through a facile liquid exfoliation method in which the assistance of H_2O_2 paved the way for easy exfoliation of bulk $MoSe_2$ into the porous structure. As-obtained hybrid nanosheets were highly suitable for HER as prerequisite of plenty of pores and irregular lateral edges. The significant improvement in edge/basal ratio was expected to enhance the active catalytic site density on $MoSe_2$/WSe_2, indicating that combination of porosity and heterostructures were useful in reducing the working overpotential [96]. Zhou *et al.* proposed a strategy to grow ternary molybdenum sulfoselenide $MoS_{2(1-x)}Se_{2x}$ with vertically aligned layers on a 3D porous nickel diselenide ($NiSe_2$) scaffold, which toked advantage of the merits of highly conductive support, double-gyroid structures and synergistic effects between two different catalysts (Fig. 7). Experimental results and quantum mechanics DFT calculation showed that these $MoS_{2(1-x)}Se_{2x}$/$NiSe_2$ hybrid catalysts exhibited an outstanding catalytic performance superior to that of the widely reported layered TMDs catalysts (especially MoS_2, WS_2 and so on). As-obtained catalysts were very effective in catalyzing hydrogen production by engineering metal dichalcogenides and pyrites into 3D hybrid architectures that possessed high surface area and abundant active edge sites [100].

The combination of TMDs with other electroactive components provides another way to overcome the sluggish HER kinetics process of TMDs-based electrocatalyts. For instance, Zhang *et al.* realized the growth of MoS_2 nanosheets on carbon paper (CP) *via* a

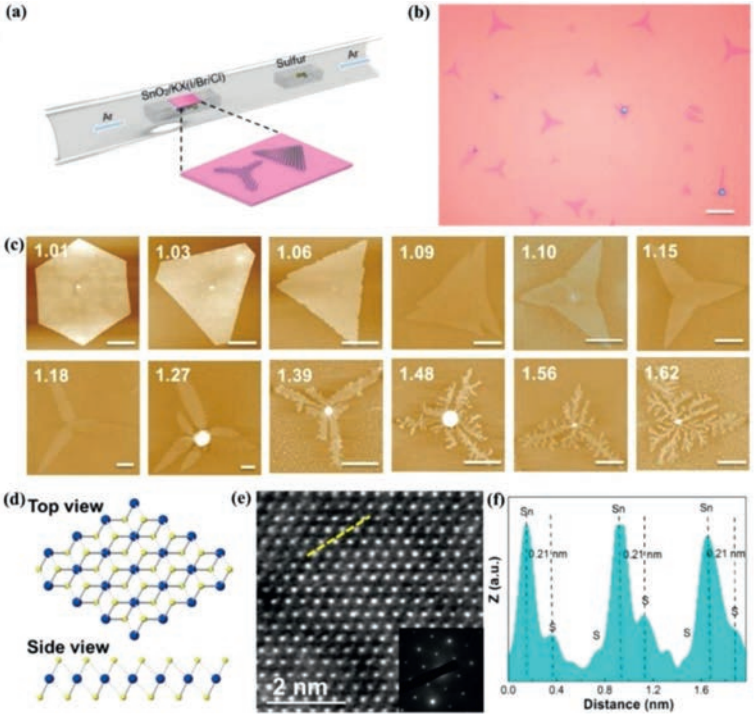

Fig. 6. Preparation of 2D SnS_2 flakes with different morphologies. (a) CVD setup for synthesis of monolayer SnS_2. (b) Typical optical image of monolayer SnS_2. Scale bar: 30 µm. (c) AFM topography images of different thickness SnS_2 with multiple morphologies. Scale bar: 5 µm. These numbers of inset represent the fractal dimension. (d) Crystal structure schematic diagram of 1T-SnS_2 in different sectional views. Sn and S atoms are colored in blue and orange, respectively. (e) HAADF-STEM image of monolayer SnS_2. Inset: corresponding SAED pattern. (f) Intensity profile of the atomic-layer SnS_2 from (e) with yellow dotted line. Reproduced with permission [94]. Copyright 2019, American Chemical Society.

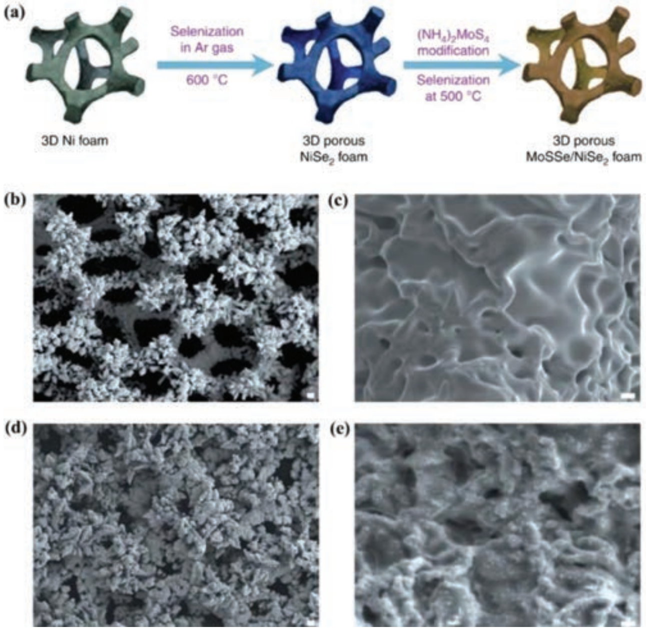

Fig. 7. The schematic diagram and morphology characterizations. (a) The procedures for growing ternary $MoS_{2(1-x)}Se_{2x}$ on porous $NiSe_2$ foam. (b, c) Typical SEM images showing the surface roughness of the $NiSe_2$ foam grown at 600 °C from commercial Ni foam. (d, e) Typical SEM images showing the morphologies of ternary $MoS_{2(1-x)}Se_{2x}$ distributed on porous $NiSe_2$ foam grown at 500 °C. (b, d) Scale bar, 50 µm. (c, e) Scale bar, 1 µm. Reproduced with permission [100]. Copyright 2016, Springer Nature.

hydrothermal method followed by the electrodeposition of amorphous $CoNi(OH)_2$ nanosheets, to form a 2D MoS_2–$CoNi(OH)_2$ hydrid. A synergistic effect deriving from the combination of MoS_2 and amorphous $CoNi(OH)_2$ facilitated HER kinetics and promoted hydrogen evolution process. Particularly, the free energy for atomic hydrogen adsorption at MoS_2 can be apparently reduced after electrodeposition of amorphous $CoNi(OH)_2$. 2D MoS_2–$CoNi(OH)_2$ presented a superior electrocatalytic performance towards HER in 0.1 mol/L KOH with a low overpotential of 178 mV at a current density of 10 mA/cm^2 and Tafel slope of 60.9 mV/dec. The current density of MoS_2–$CoNi(OH)_2$ nanocomposite for HER at the overpotential of more than 0.190 V was even higher than that of the commercial Pt/C catalyst [101]. Vikraman *et al.* adopted one-pot method to engineer the novel hybrid using a molybdenum carbide (Mo_2C) to insert $MoSe_2$ matrix. Microscopic analyses clearly suggested that Mo_2C embedded $MoSe_2$ hybrid nanoarray was formed, and the obtained nanoarray was composed of nanosized spherical grains with plenty of active sites. Improved surface area and highly conductive nature were obviously confirmed for the $MoSe_2-Mo_2C$ hybrid. The low overpotential (73 mV at 10 mA/cm^2) with a small Tafel slope (51 mV/dec) and a higher current density of 0.982 mA/cm^2 were achieved by $MoSe_2-Mo_2C$ hybrid nanoarrays for HER [95].

Currently, phase engineering has been as an effective method to tune the phase conversion and electrocatalytic properties of TMDs, the 1T phase and 1T′ phase present obviously enhanced electrocatalytic performances towards HER, due to their fast transfer of electrons and the large abundance of active sites. However, the types of TMDs with unconventional phase and the synthesis strategies are very limited (mainly focused on 1T-phase or 1T′-phase), which is desirable to explore more and more TMDs with stable unconventional phase. Furthermore, how to enhance the purity of the unconventional phase or to engineer the hybrid heterostructures with perfect contact is another key challenge.

3. Metal thiophosphate compounds

As another kind of newly developed 2D materials, metal thiophosphates (MTPs) have attracted much attention due to their fascinating structure and tunable properties. Layered MTPs are

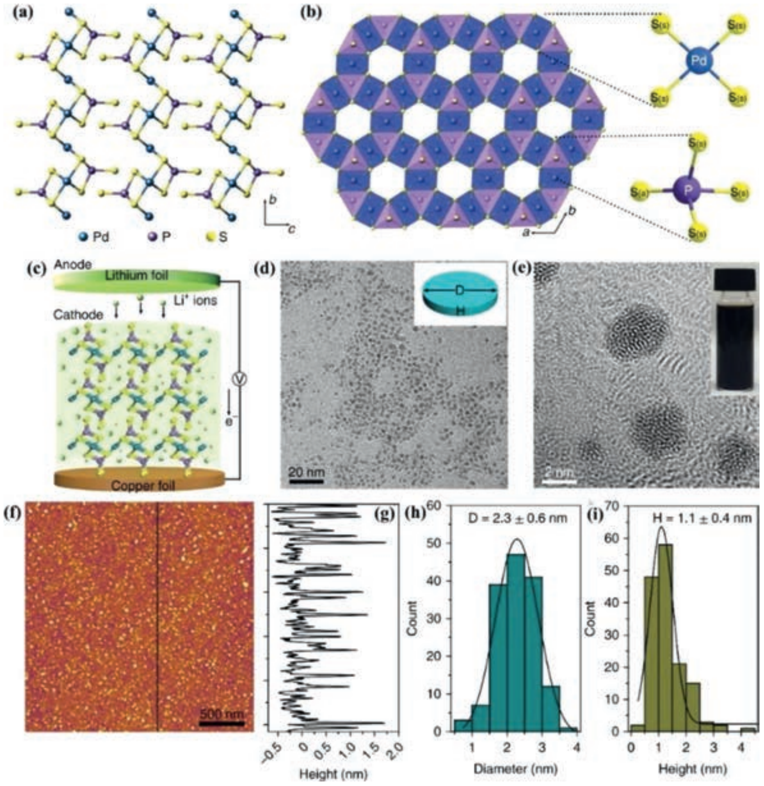

Fig. 8. Crystal structure of layered $Pd_3P_2S_8$ and the result of its electrochemical lithiation. (a) Atomic structure of three-layer building blocks of $Pd_3P_2S_8$ along the a axis. (b) Coordination polyhedra of $Pd_3P_2S_8$ viewed along the c axis. The sulfur atoms with different sites are labelled as $S_{(a)}$ (atoms at the apical position) and $S_{(s)}$ (atoms at the side position). The coordination circumstance of palladium with four equivalent sulfur atoms and the coordination circumstance of phosphorus with two types of P–S bonds are indicated. (c) Schematic illustration of the preparation of Li-PPS NDs from layered bulk $Pd_3P_2S_8$ crystals using the electrochemical lithiation method. (d) TEM and (e) high-resolution TEM images of Li-PPS NDs. Insets: a morphology sketch of Li-PPS ND (d) and a photo of Li-PPS NDs in water (e). D, diameter; H, height. (f) AFM image of Li-PPS NDs. (g) Height profile along the black line in f. (h) Statistical analysis of the sizes of 150 Li-PPS NDs measured by TEM, in which 2.3 nm is the mean size and 0.6 nm is the standard deviation (s.d.). (i) Statistical analysis of the heights of 150 Li-PPS NDs measured by AFM, in which 1.1 nm is the mean thickness and 0.4 nm is the s.d. The curves in h and i were obtained by fitting the date using a Gaussian function, and 68% of values drawn from the distribution are within one s.d. away from the mean. Reproduced with permission [105]. Copyright 2018, Springer Nature.

slightly different from TMDs due to their ternary structures in which transition metal is encapsulated by both sulfur and phosphorus atoms (a general structure of MPS_3, M = transition metal). The simultaneous presence of sulfur and phosphorous takes a synergistic effect on the surface electronic structure of center metal atoms, which has an impact on the catalytic activity. Recently, MTPs have drawn considerable interests in applications for electorcatalytic HER [102,103]. Similar to other ultrathin 2D materials, fewer-layer MTPs nanosheets are considered to have extra electrocatalytic properties rather than the corresponding bulk form [104–106]. How to realize the fewer-layer form and the phase conversion of bulk MTPs is a key factor for their practical applications in HER. For instance, ternary palladium thiophosphate ($Pd_3P_2S_8$) is a layered compound with an interlocked layered structure and waved Pd–P–S layers, however, due to its unremarkable properties, there has been no report on the exploration of $Pd_3P_2S_8$ for practical applications. Zhang *et al*. reported the amorphization of layered $Pd_3P_2S_8$ to prepare amorphous ultrasmall lithium-incorporated palladium phosphosulfide (Li-PPS) nanodots (NDs) through a controllable electrochemical lithiation process. As-obtained Li-PPS NDs possessed abundant vacancies as well as doping lithium in the Pd–P–S frameworks (Fig. 8). Such amorphization process can activate the non-electroactive $Pd_3P_2S_8$ for electrocatalytic HER. Amorphous Li-PPS NDs exhibited high HER activity and outstanding long-term stability. The activation of electrocatalytic activity of $Pd_3P_2S_8$ was attributed to its morphology and structure changes induced by lithiation process [105]. Wu *et al*. adopted a similar lithium intercalation method to synthesize $Pd_3P_2S_8$ with only few layers under mild sonication. Benefiting from the decreased dimension, 2D palladium thiophosphate nanosheets exhibited increased photoresponse intensity and photo-electron catalytic activity for both HER and OER in various pH mediums, demonstrating the superior stability in structure and chemical compositions during real application [107]. In order to avoid the low intrinsic conductivity and slow HER kinetics of bulk $FePS_3$, Yu *et al*. adopted a new amine-assisted exfoliation method to obtain few-layer nanosheets with tunable electrical conductivity. They regulated the crystallinity and structure of $FePS_3$ by the reaction temperature. When the reaction temperature was increased, the ratio of Fe^{3+}/Fe^{2+} increased and more sulfur atoms escaped from the structure in $FePS_3$ nanosheets, leading to the amorphization and more defects of sulfur to improve the intrinsic electrical conductivity of the as-exfoliated nanosheets. The combined effect of mixed valence and crystallinity resulted in superior HER performance, and a decrease of the overpotential of 147 mV and a drop of the Tafel slope from 139 mV/dec to 94 mV/dec were achieved [108].

Combining two different metal cations together to fabricate the novel MTPs hybrid is a promising strategy to enhance electrocatalytic properties for HER due to its better electrical conductivity and richer redox reactions [109–111]. For example, Wang *et al*. reported that cobalt doping of $FePS_3$ promoted intrinsic active sites for efficient HER. Enlightened by the theoretical calculations that Co dopants improved H affinity on P sites and electrical conductivity, they synthesized a series of $Fe_{1-x}Co_xPS_3$ (x = 0, 0.05, 0.1, 0.15, 0.2, 0.25) catalysts. It is shown that 15% Co doping greatly reduced the overpotential by 166 mV, and the Tafel slope decreased from

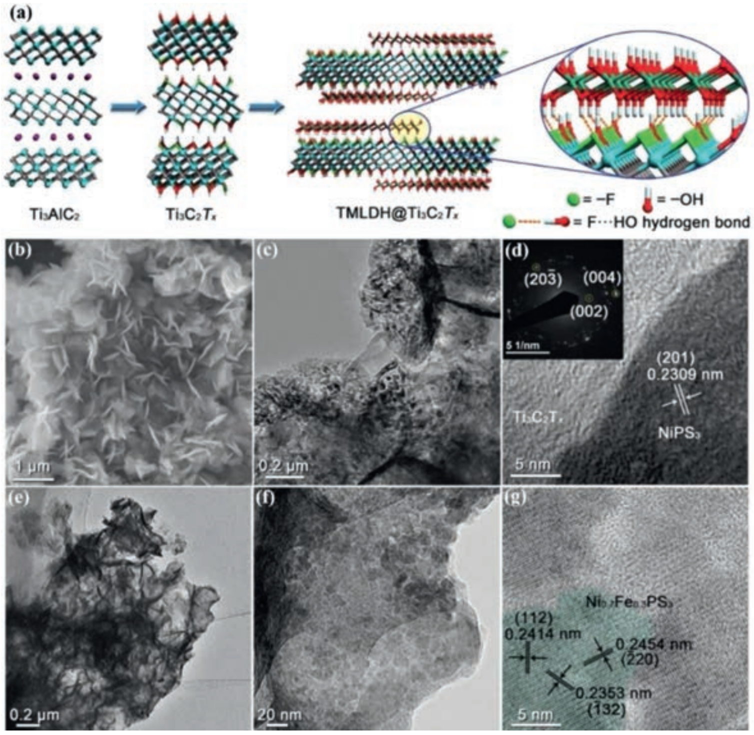

Fig. 9. (a) From left to right: the HF etching and exfoliation of $Ti_3C_2T_x$ nanosheets, and the schematic illustration of TMLDHs assemble on $Ti_3C_2T_x$ surface. The enlarged view indicating the hydrogen bond interaction between –F groups on $Ti_3C_2T_x$ and –OH groups from TMLDH. (b) SEM image and (c) TEM image of the $NiPS_3$@MXene nanosheets. (d) HRTEM of the $NiPS_3$@MXene nanosheets. Insets show the SAED pattern. (e, f) TEM images of the $Ni_{0.7}Fe_{0.3}PS_3$@MXene nanosheets. (g) The HRTEM of the $Ni_{0.7}Fe_{0.3}PS_3$@MXene nanosheets. Reproduced with permission [118]. Copyright 2018, Wiley-VCH.

170 mV/dec to 80 mV/dec [112]. Song *et al.* demonstrated highly efficient water splitting in alkaline solution using quarternary mixed nickel iron phosphosulfide ($Ni_{1-x}Fe_xPS_3$) nanosheets (NSs). With tuned electronic structure and improved electrical conductivity induced by mixing appropriate amount of Fe into $NiPS_3$, $Ni_{0.9}Fe_{0.1}PS_3$ NSs displayed excellent HER activity (an overpotential of 72 mV at the current density of −10 mA/cm^2 and a Tafel slope of 73 mV/dec) [113]. Similarly, Tang *et al.* reported the rational tuning of surface electronic structure of $FePS_3$ nanosheets by anchoring atomically dispersed metal atom. Theoretical calculations predicted that the strong electronic coupling effect in single-atom Ni-$FePS_3$ facilitated electron aggregation from Fe atom to the nearby Ni-S bond, and enhanced the electron-transfer of Ni and S sites. It can balance the oxygen species adsorption capacity, and reinforce water adsorption and dissociation process to accelerate OER and HER. Interestingly, the electrochemical tests proved that the optimal Ni-$FePS_3$ NSs exhibited outstanding electrochemical water-splitting activities, delivering an overpotential of 287 mV at the current density of 10 mA/cm^2 and a Tafel slope of 41.1 mV/dec for OER, as well as 219 mV decrease in overpotential at 10 mA/cm^2 for HER [114].

Incorporating conductive supports could further enhance electron and mass transfer as well as structural stability of MTPs during catalyzing HER [115,116]. For instance, Liang *et al.* performed the calculations with DFT to design the mosaic structured $CoNiPS_3$ nanosheets. They presented a scalable and flexible strategy to prepare single crystalline $CoNiPS_3$ incorporated with N-doped carbon ($CoNiPS_3$/C) nanosheets (∼16 nm thickness), which was further processed into the mosaic structured $CoNiPS_3$/C nanosheets. The mosaic $CoNiPS_3$/C nanosheets showed an average thickness of ∼6 nm and a lateral size of ∼130 nm. Coupled with intrinsic electronic benefits and external structural advantages, the mosaic $CoNiPS_3$/C nanosheets were as an efficient bifunctional electrocatalyst for HER/OER in 1.0 mol/L KOH, with low overpotentials of 140 mV for HER and 262 mV for OER at 30 mA/cm^2, respectively, and with Tafel slopes of 60 mV/dec for HER and 56 mV/dec for OER, respectively. It should be noted the mosaic $CoNiPS_3$/C nanosheets showed much better electrocatalytic stability due to the existence of carbon support [117]. Du *et al.* also presented a nickel-based bimetal phosphorus trisulfde ($Ni_{1-x}FexPS_3$, simplified as NFPS) mosaic that decorated on the surface of MXene nanosheets (NFPS@MXene). The nanohybrids were synthesized through a facile self-assemble process of transition metal layered double hydroxide (TMLDH) on MXene surface, followed by a low temperature *in situ* solid-state reaction step. Based on the structure analysis, the nanomosaic morphology of NFPS might be attributed to that the lattice stress generated during the solid state reaction process resulted in the *in-situ* fragmentation of NFPS from original TMLDHs nanosheets (Fig. 9). By tuning the Ni:Fe ratio, NFPS@MXene nanohybrids exhibited excellent activities as electrocatalysts for overall water splitting. The surface functional groups of MXene may interact with the MTPs to form hybrid structures and affect their surface electronic structure, which enhanced the electrocatalytic activity. Particularly, the $Ni_{0.9}Fe_{0.1}PS_3$@MXene showed low overpotential for the hydrogen evolution reaction (HER) in 1 mol/L KOH solution [118].

Although MTPs display great potential in catalyzing HER, various fundamental problems remain unsolved. The tuning process of MTPs conductivity is not well explained at present, and how to improve its intrinsic conductivity is a key factor to further exploit its potential properties for catalyzing HER. The successful exfoliation of less-layer MTPs has not been well conducted, particularly, the electrical conductivity of MTPs is closely related with fewer-layer structure. So the synthesis, structure, properties and application of MTPs should be deeply explored in the future.

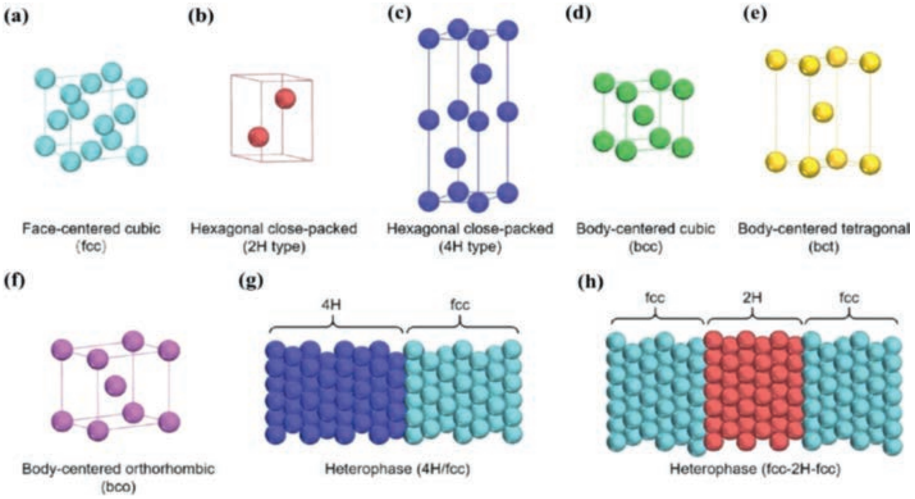

Fig. 10. Atomic models of different crystal phases and crystal phase-based heterostructures of Au nanomaterials: (a) fcc; (b) 2H; (c) 4H; (d) bcc; (e) bct; (f) bco; (g) 4H/fcc heterophase; (h) fcc/H/fcc heterophase. Reproduced with permission [119]. Copyright 2020, American Chemical Society.

4. 2D noble metal nanomaterials

4.1. Au-based nanosheets

2D noble metal nanomaterials with unique phases have exhibited interesting structural and chemical properties which are distinctive from their bulk counterparts and expand their applications for energy conversion and catalysis [27,28,119,120]. Controlling crystal structures through phase engineering to prepare 2D noble metal nanomaterials with unconventional phases is highly desirable due to their unique electrocatalytic properties [51,52,121-123]. In the past years, various methods have been developed to synthesize different Au nanostructures, including nanorods, nanoplates, nanowires, nanoribbons and nanopolyhedra. However, the vast majority of reported Au nanomaterials are traditional face-centered cubic (fcc) phase, which exhibits a characteristic packing sequence of "ABC" in the close-packed $[111]_f$ direction (Fig. 10a). Fortunately, phase engineering has provided a significant and efficient approach to modulate physicochemical properties of Au nanomaterials [51,52,124,125]. With the development of synthetic techniques, 2H (hexagonal close-packed), 4H (hexagonal close-packed), bcc (body centered cubic), bct (bodycentered tetragonal) and bco (body-centered orthorhombic) phase Au nanomaterials have been synthesized (Figs. 10b–f). In addition, unique Au nanostructures with heterophases, such as 4H/fcc and fcc–2H–fcc (Figs. 10g and h) were also synthesized, which can be viewed as the assembly of different phases. Recent studies have confirmed that crystal phase was significantly related with electrochemical properties of Au nanomaterials [126,127]. For instance, Fan *et al*. used a colloidal synthesis method to synthesize hexagonal 4H Au nanoribbon (NRB). It was observed that 4H phase of Au NRBs can be transformed to fcc phase through ligand exchange under ambient conditions. The simulated and observed electron energy-loss spectroscopy (EELS) on a single Au NRB demonstrated that the optical response of 4H Au NRB was quite different to that of fcc Au NRB [50]. They also successfully synthesized a novel class of noble multimetallic nanomaterials, *i.e.*, 4H/fcc Au@PdAg, Au@PtAg, and Au@PtPdAg core–shell NRBs by galvanic reaction method (Fig. 11a). 4H/fcc Au@PdAg NRBs as a novel electrocatalyst for HER, exhibited excellent catalytic performance close to that of commercial Pt black [128]. Furthermore, they firstly prepared 2D square-like Au nanosheets with an unconventional 2H/fcc heterophase, and used them as templates to grow one-dimensional (1D) Rh nanorods. By tuning reaction conditions, they prepared three types of 1D/2D Rh–Au heterostructures as illustrated in Fig. 11b. In the type A heterostructure, Rh nanorods only grew on the fcc defects including stacking faults and/or twin boundaries (denoted as fcc-SF/T) and 2H phases in two 2H/fcc edges of the Au nanosheet (Fig. 11b). In the type B heterostructure, Rh nanorods grew on the fcc-SF/T and 2H phases in two 2H/fcc edges and two 2H/fcc basal planes of the Au nanosheet (Fig. 11b). In the type C heterostructure, Rh nanorods grew on four edges and two basal planes of the Au nanosheet (Fig. 11b). The anisotropic morphologies and coherent interfaces in type C resulted in the formation of a continuous network, favoring the enhanced electrochemically active surface

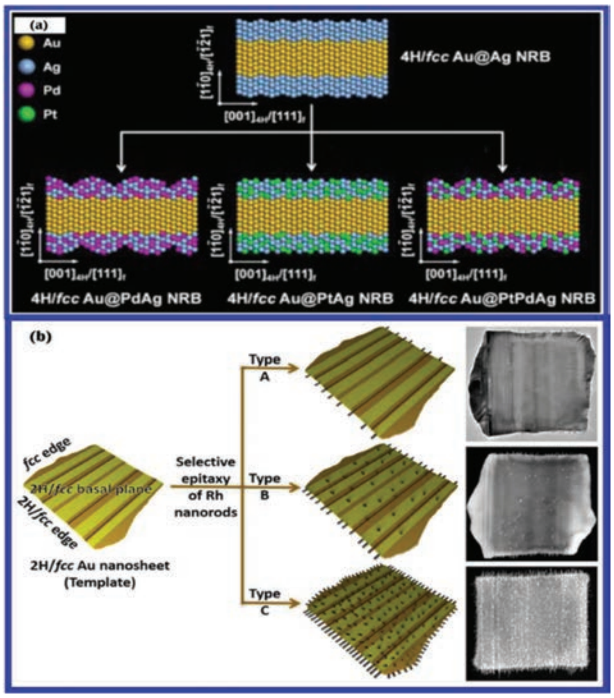

Fig. 11. (a) 4H/fcc Au@PdAg, Au@PtAg, and Au@PtPdAg core–shell NRBs were synthesized from 4H/fcc bimetallic Au@Ag core–shell NRBs *via* galvanic reaction of Ag with $Pd(NO_3)_2$, $Pt(NO_3)_2$, and a mixture of $Pt(NO_3)_2$ and $Pd(NO_3)_2$ (from right to left), respectively. Reproduced with permission [128]. Copyright 2016, American Chemical Society. (b) Construction of three types of 1D/2D Rh–Au heterostructures by using 2H/fcc heterophase Au nanosheets as templates. Reproduced with permission [125]. Copyright 2021, American Chemical Society.

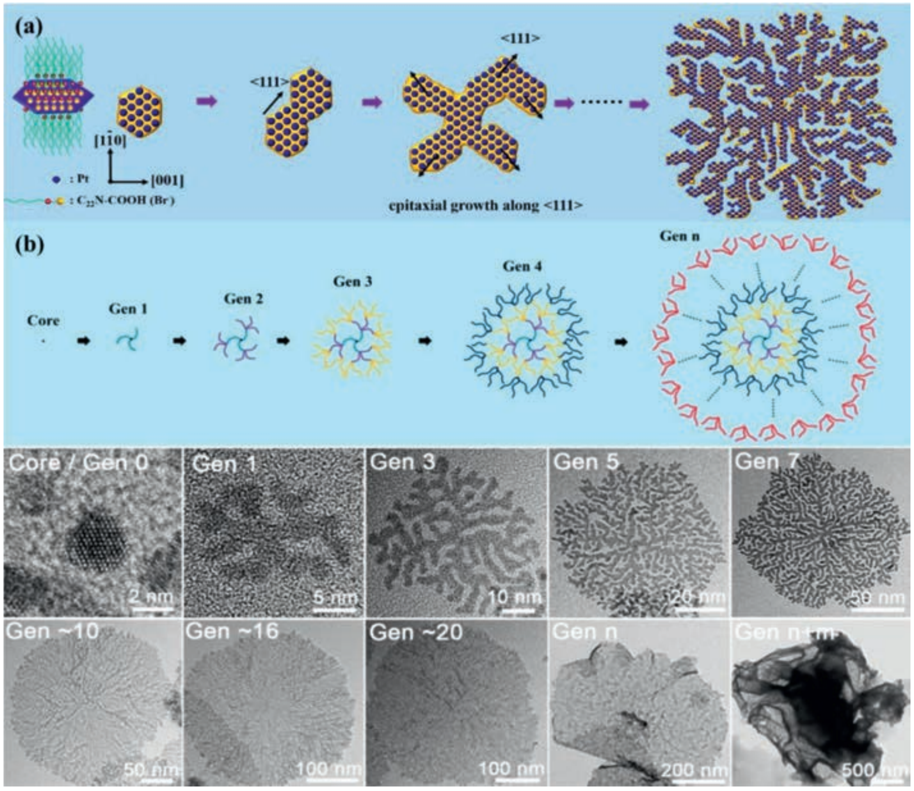

Fig. 12. (a) Proposed formation mechanism for crystalline facet-directed step-by-step in-the-plane epitaxial growth of Gen-7 PtNDs selectively along the ⟨111⟩ crystallographic orientation. (b) Schematics and corresponding TEM images of 2D inorganic PtNDs at different generations. Reproduced with permission [134]. Copyright 2019, American Chemical Society.

areas and oriented transport of electrons, so the type C heterostructure showed a promising performance toward electrochemical HER in acidic media [125]. Similarly, Lu *et al.* used 4H/fcc Au nanowires (NWs) as seeds to epitaxially grow Ru and Rh nanorods (NRs), and realized epitaxial growth of Ru nanorods on the 4H phase and fcc-twin boundary in Au nanowires. The resultant Ru NRs could also serve as nucleation sites for further growth of Rh NRs to form Au–Ru–Rh hybrid NWs. The controlled overgrowth relied on highly active 4H and fcc-twin structures in the 4H/fcc Au NWs. 4H/fcc Au–Ru NWs as electrocatalysts for HER in alkaline media gave a high turnover frequency (TOF) of 0.31 H_2 s^{-1} at 50 mV overpotential [129].

4.2. Non Au-based 2D noble metal nanomaterials

Electrocatalytic properties of non Au-based 2D crystalline metal nanomaterials can be also modulated by their phase engineering [130–133]. For instance, inspirited by the synthesis of 4H Au nanoribbons and 4H/fcc Au nanorods with crystal-phase heterostructure, Lu *et al.* reported the synthesis of hierarchical 4H/fcc Ru nanotubes (NTs) through the seeded growth followed by selective chemical etching. Hierarchical 4H/fcc Ru NTs containing ultrathin Ru shells (5–9 atomic layers) and tiny Ru nanorods (NRs) with the length of 4.2 ± 1.1 nm and diameter of 2.2 ± 0.5 nm vertically on the surface of Ru shells can be obtained. The hierarchical 4H/fcc Ru NTs showed a higher exchange current density of 1.81 mA/cm^2 as well as lower overpotential of 23 mV at 10 mA/cm^2 than 4H/fcc Au-Ru NWs, commercial Pt/C and Ru/C [57]. Xu *et al.* presented 2D ultrathin single-crystalline platinum NDs through a surfactant-directed solution-phase synthesis under ambient conditions. The long-chain amphiphilic surfactant with quaternary ammonium and carboxyl functional heads was used as a structure-directing template, and halide counterion of Br$^-$ acted as facet-capping agent. This combination was the key factor to kinetically control in-the-plane epitaxial growth of metal nanocrystals along selectively exposed crystalline facets (Fig. 12a). Step-by-step growth of PtNDs was well controlled by systematically tuning the concentrations and feed ratios of surfactant template and metal precursor as well as reduction kinetics. The generation of ultrathin PtNDs was readily tuned in the range from Gen 0 (core, 2 nm) to ~Gen 25 (~500 nm) and even to >Gen 50 (>1000 nm) in which the average length of one generation was about 20 nm as illustrated in Fig. 12. Since 2D single crystalline Pt ND nanostructures exposed more catalytically active sites and thus kinetically facilitated mass/electron transfers during electrocatalysis, PtNDs exhibited superior electrocatalytic performance in HER [134]. The exploiting of Pt-based bimetals with unconventional crystal phases is also a promising approach for developing noble metal-based nanomaterials with enhanced or new functionalities. For instance, Cao *et al.* have synthesized Ni-rich Pt–Ni alloy nano-multipods in the unusual hcp (hexagonal close-packed) phase. The building blocks of the multipods were highly concaved hexagonal prisms assembled by six nanosheets (about 2.5 nm in thickness) with exposed high energy facets, which endowed nano-multipods with a large surface area. Control studies exhibited that formaldehyde in the growth solution played the pivotal role in formation of the unique hcp structure. Particularly, the formation of excavated polyhedral morphology was attributed to the preferential deposition of Pt atom on the edge of the solid branch of hcp Pt–Ni alloy, followed by the diffusion of face-sited Ni atoms to the edges. The hcp Pt–Ni excavated nano-multipods exhibited superior catalytic property towards HER in alkaline electrolyte. The overpotential was 65 mV at a current density of 10 mA/cm^2, and the mass current density reached 3.03 mA/mg$_{Pt}$ at −70 mV *vs.* RHE [135].

2D noble metal nanomaterials with unconventional phases demonstrate superior catalytic performances over the common fcc counterparts in catalyzing HER, however, the formation mechanism of unconventional phases and the relation between phase changing and catalytic properties are yet not clear, which is necessary to be deeply discussed with the aid of novel characterization and complex theoretical calculation. It should be noted that the discovered unconventional phases on noble metals are quite limited, particularly, the unconventional phases originating from the other noble metal (such as Pd, Ag, Rh) are very scarce, which is urgent for further exploration.

5. Challenges and perspectives

In summary, the recent development of phase engineering of two-dimensional nanomaterials for applications in electrocatalytic HER is summarized. Although considerable progress on their synthesis and application for HER has been made, there are still many challenges in the controlled synthesis, fundamental understanding and electrocatalytic applications. Firstly, phase engineering-derived 2D nanomaterials are difficult to obtain due to high surface energy in 2D morphology and unconventional phase, so the types and the facile and scale-up strategies for 2D nanomaterials are very limited. Especially, it is very challenging to synthesize 2D nanomaterials with a pure unconventional phase to fully release their catalytic capacity. Secondly, the fundamental insight toward the formation and stabilization of unconventional phases still remains unclear. More and more *in situ* techniques should be used to monitor the formation process of unconventional phases. Particularly, the theoretical calculation and simulation are urgently required to understand the formation and stabilization mechanisms of unconventional phases. Thirdly, the relationship between phase and property of 2D nanomaterials is still unclear. More and more novel 2D nanomaterials with different size, thickness, shapes and crystal phases are expected to be synthesized to discover phase-dependent properties. Especially, how to realize rational design of well-defined nanostructures through phase engineering technology is also challengeable, which may be in favor of qualitatively discovering the correlations between structural features and properties. Last but not least, there are still many challenges related with the practical application of these materials toward HER. Particularly, some novel unconventional phases may be not stable for their practical applications under strong acid and strong alkali. So one of the most urgent challenges is to explore simple but reliable methods to stabilize phase engineering-derived 2D nanomaterials during practical application.

The rapid development of artificial intelligence, advanced material characterization technique and complex theoretical calculation will provide a huge opportunity for the researchers to predict more new unconventional phases. So it is anticipated that many more intriguing unconventional phases will be discovered and the scalable production of highly stable new phases will be realized in the future, and their deeper application in industrial HER is an unavoidable tendency. How to comprehensively and systematically access the electrocatalytic performances of phase engineering-derived 2D nanomaterials in the practical application is a key factor, which will promote the wider replacement of Pt-based catalysts with unconventional phases-based catalysts in the industry of H_2 generation.

Declaration of competing interest

The authors declare that they have no known competing financial interests or personal relationships that could have appeared to influence the work reported in this paper.

Acknowledgments

This work was financially supported by the Key Grant for Special Professors in Jiangsu Province (No. RK030STP18001), the Scientific Research Foundation of Nanjing University of Posts and Telecommunications (No. NY218150), “1311 Talents Program” of Nanjing University of Posts and Telecommunications and the National Postdoctoral Program for Innovative Talents (No. BX20190156).

References

[1] N. Cheng, S. Stambula, D. Wang, et al., Nat. Commun. 7 (2016) 13638.
[2] D. Zhang, H. Mou, F. Lu, C. Song, D. WAng, Appl. Catal. B 254 (2019) 471–478.
[3] D.W. Boukhvalov, Y.W. Son, R.S. Ruoff, ACS Catal. 4 (2014) 2016–2021.
[4] X. Zou, Z. Li, Y. Xie, H. Wu, S. Lin, Int. J. Hydrogen Energy 45 (2020) 30647–30658.
[5] Z. Li, X. Huang, X. Zhang, L. Zhang, S. Lin, J. Mater. Chem. 22 (2012) 23602–23607.
[6] Z. Li, L. Zhang, X. Huang, L. Ye, S. Lin, Electrochim. Acta 121 (2014) 215–222.
[7] Z. Li, S. Lin, Z. Chen, Y. Shi, X. Huang, J. Colloid Interface Sci. 368 (2012) 413–419.
[8] S. Ye, F. Luo, Q. Zhang, et al., Energy Environ. Sci. 12 (2019) 1000–1007.
[9] Z. Gao, M. Li, J. Wang, et al., Carbon 139 (2018) 369–377.
[10] M.J. Muñoz-Batista, D. Motta Meira, G. Colón, A. Kubacka, M. Fernández-García, Angew. Chem. Int. Ed. 57 (2018) 1199–1203.
[11] X. Wang, L. Zhuang, Y. Jia, et al., Angew. Chem. Int. Ed. 57 (2018) 16421–16425.
[12] W. Wu, C. Niu, C. Wei, et al., Angew. Chem. Int. Ed. 58 (2019) 2029–2033.
[13] P. Wang, X. Zhang, J. Zhang, et al., Nat. Commun. 8 (2017) 14580.
[14] Q. Lu, Y. Yu, Q. Ma, B. Chen, H. Zhang, Adv. Mater. 28 (2016) 1917–1933.
[15] L. Lin, P. Sherrell, Y. Liu, et al., Adv. Energy Mater. 10 (2020) 1903870.
[16] L. Najafi, S. Bellani, R. Oropesa-Nuñez, et al., Adv. Energy Mater. 8 (2018) 1703212.
[17] C.H. Choi, M. Kim, H.C. Kwon, et al., Nat. Commun. 7 (2016) 10922.
[18] J. Deng, P. Ren, D. Deng, X. Bao, Angew. Chem. Int. Ed. 54 (2015) 2100–2104.
[19] Y.C. Chen, A.Y. Lu, P. Lu, et al., Adv. Mater. 29 (2017) 1703863.
[20] S. Park, C. Kim, S.O. Park, et al., Adv. Mater. 32 (2020) 2001889.
[21] S.S. Nishat, M.T. Islam, S. Ahmed, A. Kabir, Mater. Today, Commun. 25 (2020) 101602.
[22] Y. Yan, P. Wang, J. Lin, J. Cao, J. Qi, J. Energy Chem. 58 (2021) 446–462.
[23] Y. Jiao, Y. Zheng, K. Davey, S. Qiao, Nat. Energy 1 (2016) 16130.
[24] L. Chang, Z. Sun, Y.H. Hu, Electrochem. Energ. Rev. 4 (2021) 194–218.
[25] C. Chang, W. Chen, Y. Chen, et al., Acta Phys. Chim. Sin. 37 (2021) 2108017.
[26] H. Li, X. Zhou, W. Zhai, et al., Adv. Energy Mater. 10 (2020) 2002019.
[27] J. Liu, Q. Ma, Z. Huang, G. Liu, H. Zhang, Adv. Mater. 31 (2019) 1800696.
[28] Y. Chen, Z. Fan, Z. Zhang, et al., Chem. Rev. 118 (2018) 6409–6455.
[29] C. Tan, X. Cao, X.J. Wu, et al., Chem. Rev. 117 (2017) 6225–6331.
[30] J. Xu, J. Zhang, W. Zhang, C.S. Lee, Adv. Energy Mater. 7 (2017) 1700571.
[31] T.A. Shifa, F. Wang, Y. Liu, J. He, Adv. Mater. 31 (2019) 1804828.
[32] R. Tong, K.W. Ng, X. Wang, et al., J. Mater. Chem. A 8 (2020) 23202–23230.
[33] Z. Liu, X. Zhang, Y. Gong, et al., Nano Res. 12 (2019) 1301–1305.
[34] J. Ping, Y. Wang, Q. Lu, et al., Adv. Mater. 28 (2016) 7640.
[35] M. Zhao, Y. Huang, Y. Peng, et al., Chem. Soc. Rev. 47 (2018) 6267–6295.
[36] L. Niu, J.N. Coleman, H. Zhang, et al., Small 12 (2016) 272–293.
[37] J. Jiang, N. Li, J. Zou, et al., Chem. Soc. Rev. 48 (2019) 4639–4654.
[38] G. Zhang, H. Liu, J. Qu, J. Li, Energy Environ. Sci. 9 (2016) 1190–1209.
[39] Z. Li, S. Xu, Y. Shi, et al., Chem. Eng. J. 414 (2021) 128814.
[40] Z. Li, S. Xu, Y. Xie, Y. Wang, S. Lin, Electrochim. Acta 264 (2018) 53–60.
[41] T. Wu, H. Zhang, Angew. Chem. Int. Ed. 54 (2015) 4432–4434.
[42] Z. Lai, A. Chaturvedi, Z. Shi, et al., Small 17 (2021) 2006866.
[43] L. Zhao, B. Dong, S. Li, et al., ACS Nano 11 (2017) 5800–5807.
[44] W. Zhai, T. Xiong, Z. He, et al., Adv. Mater. 33 (2021) 2006661.
[45] Q. Song, J. Wang, Q. Sun, et al., Chem. Commun. 56 (2020) 10285–10288.
[46] H.F. Shen, Z.W. Shao, Q.F. Zhao, et al., J. Colloid Interface Sci. 573 (2020) 115–122.
[47] K. Sun, Y. Liu, Y. Pan, et al., Nano Res. 11 (2018) 4368–4379.
[48] Q. Zhou, G. Zhao, K. Rui, et al., Nanoscale 11 (2019) 717–724.
[49] X. Zhang, H. Cheng, H. Zhang, Adv. Mater. 29 (2017) 1701704.
[50] Z. Fan, M. Bosman, X. Huang, et al., Nat. Commun. 6 (2015) 7684.
[51] Z. Fan, X. Huang, Y. Han, et al., Nat. Commun. 6 (2015) 6571.
[52] X. Huang, S. Li, Y. Huang, et al., Nat. Commun. 2 (2011) 292.
[53] Y. Ge, Z. Shi, C. Tan, et al., Chem 6 (2020) 1237–1253.
[54] H.H. Huang, X. Fan, D.J. Singh, W.T. Zheng, Nanoscale 12 (2020) 1247–1268.
[55] Y. Chen, Z. Lai, X. Zhang, et al., Nat. Rev. Chem. 4 (2020) 243–256.
[56] H. Jin, Q. Gu, B. Chen, et al., Chem 6 (2020) 2382–2394.
[57] Q. Lu, A. Wang, H. Cheng, et al., Small 14 (2018) 1801090.
[58] Y. Zheng, P. Wu, M. Gao, et al., Nat. Commun. 9 (2018) 2533.
[59] Z. Lei, J. Zhan, L. Tang, Y. Zhang, Y. Wang, Adv. Energy Mater. 8 (2018) 1703482.
[60] J. Shi, X. Wang, S. Zhang, et al., Nat. Commun. 8 (2017) 958.
[61] J. Ping, Z. Fan, M. Sindoro, Y. Ying, H. Zhang, Adv. Funct. Mater. 27 (2017) 1605817.

[62] H. Huang, J. Zha, S. Li, C. Tan, Chin. Chem. Lett. 33 (2022) 163–176.
[63] T. Rao, H. Wang, Y.J. Zeng, et al., Adv. Sci. 8 (2021) 2002284.
[64] J. Yi, X. She, Y. Song, et al., Chem. Eng. J. 335 (2018) 282–289.
[65] Q. He, Z. Wang, L. Meng, Q. Chen, G. Yong, Chem. J. Chin. Univ. 42 (2021) 523–538.
[66] W. Jia, X. Zhou, Y. Huang, et al., ChemCatChem 11 (2019) 707–714.
[67] X. Zhang, H. Li, H. Yang, et al., ChemElectroChem 7 (2020) 3347–3352.
[68] X. Zheng, G. Zhang, X. Xu, et al., Appl. Surf. Sci. 496 (2019) 143694.
[69] L. Zhang, K. Wei, J. Yin, et al., Langmuir 36 (2020) 14342–14351.
[70] Y. Xu, R. Wang, J. Wang, et al., Chem. Eng. J. 417 (2021) 129233.
[71] L. Zhang, K. Wei, J. Ma, et al., Appl. Surf. Sci. 566 (2021) 150754.
[72] Z. Zhou, X. Wang, H. Zhang, et al., Small 17 (2021) 2007486.
[73] Y. Li, K.A.N. Duerloo, K. Wauson, E.J. Reed, Nat. Commun. 7 (2016) 10671.
[74] S.K. Kim, W. Song, S. Ji, et al., Appl. Surf. Sci. 425 (2017) 241–245.
[75] D. Han, Z. Luo, Y. Li, et al., Appl. Surf. Sci. 529 (2020) 147117.
[76] J. Ekspong, E.Gracia Espino, Adv. Theory Simul. 3 (2020) 1900213.
[77] W. Chen, J. Gu, Y. Du, et al., Adv. Funct. Mater. 30 (2020) 2000551.
[78] X. Xu, R. Zhao, W. Ai, et al., Adv. Mater. 30 (2018) 1800658.
[79] B. Chen, H. Bi, Q. Ma, et al., Sci. China Mater. 60 (2017) 1102–1108.
[80] A.G. del Águila, S. Liu, T.Thu Ha Do, et al., ACS Nano 13 (2019) 13006–13014.
[81] U. Krishnan, M. Kaur, K. Singh, M. Kumar, A. Kumar, Superlattices Microstruct. 128 (2019) 274–297.
[82] Z. Zhou, B. Li, C. Shen, et al., Small 16 (2020) 2004173.
[83] M. Deng, M. Li, H.G. Park, ACS Appl. Energy Mater. 1 (2018) 5993–5998.
[84] H. Mao, Y. Fu, H. Yang, et al., ACS Appl. Mater. Interfaces 12 (2020) 25189–25199.
[85] M.A. Lukowski, A.S. Daniel, F. Meng, et al., J. Am. Chem. Soc. 135 (2013) 10274–10277.
[86] Y. Yu, G.H. Nam, Q. He, et al., Nat. Chem. 10 (2018) 638–643.
[87] D. Wang, X. Zhang, S. Bao, et al., J. Mater. Chem. A 5 (2017) 2681–2688.
[88] Y. He, P. Tang, Z. Hu, et al., Nat. Commun. 11 (2020) 57.
[89] C. Tan, Z. Luo, A. Chaturvedi, et al., Adv. Mater. 30 (2018) 1705509.
[90] Q. Fu, J. Han, X. Wang, et al., Adv. Mater. 33 (2021) 1907818.
[91] L. Xie, L. Wang, W. Zhao, et al., Nat. Commun. 12 (2021) 5070.
[92] Z. Lai, A. Chaturvedi, Y. Wang, et al., J. Am. Chem. Soc. 140 (2018) 8563–8568.
[93] J. Li, M. Hong, L. Sun, et al., ACS Appl. Mater. Interfaces 10 (2018) 458–467.
[94] G. Shao, X.X. Xue, X. Zhou, et al., ACS Nano 13 (2019) 8265–8274.
[95] D. Vikraman, S. Hussain, K. Karuppasamy, et al., Appl. Catal. B 264 (2020) 118531.
[96] H.Singh Rahul, N.P. Lalla, U. Deshpande, S.K. Arora, Mater. Today Proc. 45 (2021) 4787–4791.
[97] L. Jia, C. Li, Y. Zhao, et al., Nanoscale 11 (2019) 23318–23329.
[98] J. Chen, X.J. Wu, Q. Lu, et al., Small 17 (2021) 2006135.
[99] Y. Han, H. Li, M. Zhang, et al., Appl. Surf. Sci. 495 (2019) 143606.
[100] H. Zhou, F. Yu, Y. Huang, et al., Nat. Commun. 7 (2016) 12765.
[101] Y. Zhang, L. Xue, C. Liang, et al., Appl. Surf. Sci. 561 (2021) 150079.
[102] J. Kibsgaard, T.F. Jaramillo, Angew. Chem. Int. Ed. 53 (2014) 14433–14437.
[103] G. Hu, J. Xiang, J. Li, et al., J. Catal. 371 (2019) 126–134.
[104] D. Mukherjee, P.M. Austeria, S. Sampath, ACS Energy Lett. 1 (2016) 367–372.
[105] X. Zhang, Z. Luo, P. Yu, et al., Nat. Catal. 1 (2018) 460–468.
[106] M. Zhu, H. Kou, K. Wang, et al., Mater. Horiz. 7 (2020) 3131–3160.
[107] B. Wu, R. Kempt, E. Kovalska, et al., ACS Appl. Nano Mater. 4 (2021) 441–448.
[108] Z. Yu, J. Peng, Y. Liu, et al., J. Mater. Chem. A 7 (2019) 13928–13934.
[109] M. Yao, H. Hu, B. Sun, et al., Small 15 (2019) 1905201.
[110] Y. Xue, M. Sun, Int. J. Hydrogen Energy 44 (2019) 16378–16386.
[111] D. Rakov, Y. Li, S. Niu, P. Xu, J. Alloys Compd. 769 (2018) 532–538.
[112] S. Wang, B. Xiao, S. Shen, et al., Nanoscale 12 (2020) 14459–14464.
[113] B. Song, K. Li, Y. Yin, et al., ACS Catal. 7 (2017) 8549–8557.
[114] C. Tang, D. He, N. Zhang, et al., Energy Environ. Mater. 5 (2022) 899–905.
[115] D.J. Li, J. Kang, H.J. Lee, et al., Adv. Energy Mater. 8 (2018) 1702806.
[116] Y. Li, S. Niu, D. Rakov, et al., Nanoscale 10 (2018) 7291–7297.
[117] Q. Liang, L. Zhong, C. Du, et al., Adv. Funct. Mater. 28 (2018) 1805075.
[118] C.F. Du, K.N. Dinh, Q.H. Liang, et al., Adv. Energy Mater. 8 (2018) 1801127.
[119] S. Lu, J. Liang, H. Long, et al., Acc. Chem. Res. 53 (2020) 2106–2118.
[120] Y. Chen, Z. Fan, J. Wang, et al., J. Am. Chem. Soc. 142 (2020) 12760–12766.
[121] Z. Fan, Z. Luo, Y. Chen, et al., Small 12 (2016) 3908–3913.
[122] Y. Chen, Z. Fan, Z. Luo, et al., Adv. Mater. 29 (2017) 1701331.
[123] Z. Fan, M. Bosman, Z. Huang, et al., Nat. Commun. 11 (2020) 3293.
[124] Z. Fan, Y. Zhu, X. Huang, et al., Angew. Chem. Int. Ed. 54 (2015) 5672–5676.
[125] J. Liu, W. Niu, G. Liu, et al., J. Am. Chem. Soc. 143 (2021) 4387–4396.
[126] W. Niu, J. Liu, J. Huang, et al., Nat. Commun. 10 (2019) 2881.
[127] C. Tan, H. Zhang, Nat. Commun. 6 (2015) 7873.
[128] Z. Fan, Z. Luo, X. Huang, et al., J. Am. Chem. Soc. 138 (2016) 1414–1419.
[129] Q. Lu, A.L. Wang, Y. Gong, et al., Nat. Chem. 10 (2018) 456–461.
[130] Y. Ge, Z. Huang, C. Ling, et al., J. Am. Chem. Soc. 142 (2020) 18971–18980.
[131] N. Yang, Z. Zhang, B. Chen, et al., Adv. Mater. 29 (2017) 1700769.
[132] Z. Zhang, Z. Luo, B. Chen, et al., Adv. Mater. 28 (2016) 8712–8717.
[133] J. Wang, J. Zhang, G. Liu, et al., Nano Res. 13 (2020) 1970–1975.
[134] D. Xu, H. Lv, H. Jin, et al., J. Phys. Chem. Lett. 10 (2019) 663–671.
[135] Z. Cao, Q. Chen, J. Zhang, et al., Nat. Commun. 8 (2017) 15131.